CENTRAL ASIAN JOURNAL OF THEORETICAL AND APPLIED SCIENCE

https://cajotas.casjournal.org/index.php/cajotas

Volume: 07 Issue: 03 | July 2026 ISSN: 2660-5317

Article

Kinetic and Thermodynamic Insights into Oxygen Evolution Reaction on Defect-Engineered Metal Oxide Nanocatalysts

Zeena Tariq Khattab [1], Rahma Abdul Hameed Hasan [2], Saad Salman Attallah [3]

1. Department of Chemistry, College of Education for Pure Sciences, Tikrit University, Iraq
2. Department of Chemistry, College of Education for Pure Sciences, Tikrit University, Iraq
3. Al-Dur Education Department, Salah al-Din Education Directorate, Ministry of Education, Iraq.

* Correspondence: zeena.tariq@tu.edu.iq

Abstract: Developing sustainable hydrogen production from water electrolysis is an important topic in which the design of earth-abundant, high-performance electrocatalysts for the oxygen evolution reaction (OER) remains a central challenge. We have synthesized oxygen vacancy-enriched iron–nickel composite oxide nanocatalysts Ov-Fe_2O_3/NiO from Iraqi natural hematite sourced from Derbendikhan district of Sulaymaniyah. In this work, we report. The preparation of catalysts occurred via alkaline co-precipitation and following hydrothermal crystallisation and thermal annealing in dilute H_2/Ar. Using X-ray diffraction (XRD), BET surface area, transmission electron microscopy (TEM), X-ray photoelectron spectroscopy (XPS), Raman spectroscopy and electron paramagnetic resonance (EPR) characterisation the oxygen vacancy defects were confirmed to be introduced in the material and a successful hetero-structure with a surface area of 78.3 m^2 g^{-1} (crystallite size 12.4 nm). In alkaline electrolyte (1 M KOH), the Ov-Fe_2O_3/NiO composite achieved an overpotential of 285 mV at a standard 10 mA cm^{-2} current density, a Tafel slope of 48 mV dec^{-1}, and a charge-transfer resistance of 3.2 Ω, which are all significantly superior to those of the undoped composite, single-phase oxides, and the reference IrO_2 catalyst. The scientists conducted electrochemical measurements of the selected nickel catalyst at 298–338 K. This enabled them to carry out rigorous kinetic analysis using the Arrhenius and Eyring formalism. The analysis yielded an activation energy of 28.4 kJ mol^{-1}, an enthalpy of activation of 25.9 kJ mol^{-1}, and an entropy of activation of −48.3 J mol^{-1} K^{-1} for the defect-engineered catalyst. The above values reflect lower barriers relative to those of the reference materials. Based on findings related to density of states reasons and XPS analysis, these thermodynamic characteristics suggest that the presence of oxygen vacancies boosts the adsorption of reactive oxygen intermediates while improving the efficiency of charge carriers and reducing O–O bond intrinsic kinetic barriers. This research provides a way to quantify designed structural defects in relation to the thermodynamic landscape of OER catalysis and shows that locally sourced Iraqi mineral precursors can serve as a feedstock for advanced manufactured electrocatalysts.

Keywords: oxygen evolution reaction; defect engineering; metal oxide nanocatalysts; oxygen vacancies; electrochemical kinetics; thermodynamic activation parameters; Iraqi natural hematite; water splitting

Citation: Khattab, Z. T, Hasan, R. A. H & Attallah, S. S. Kinetic and Thermodynamic Insights into Oxygen Evolution Reaction on Defect-Engineered Metal Oxide Nanocatalysts. Central Asian Journal of Theoretical and Applied Science 2026, 7(3), 24-36

Received: 10th Feb 2026
Revised: 21th Mar 2026
Accepted: 18th Apr 2026
Published: 11th May 2026

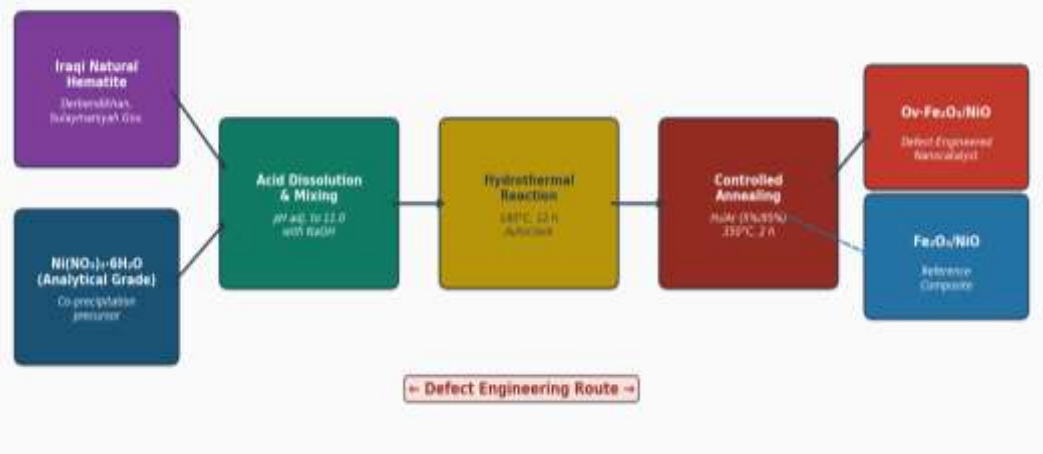

Figure 1. Schematic representation of the synthesis and defect engineering workflow for Ov-Fe_2O_3/NiO nanocatalysts derived from Iraqi natural hematite (Derbendikhan district, Sulaymaniyah Governorate, Iraq).

1. Introduction

The global demand for clean energy is on the rise. Additionally, there is a growing need to decarbonise industrial processes. As a result, experts say electrochemical water splitting is one of the most technically and scientifically convincing ways to achieve sustainable hydrogen generation. The anodic oxygen evolution reaction (OER) is the main thermodynamic and kinetic bottleneck within this two-electrode process. Water can be oxidized to molecular oxygen in a four-electron, four-proton manner, which has a theoretical standard potential of 1.23 V versus the reversible hydrogen electrode (RHE). However, in reality, overpotentials of > 250–400 mV are typically required to generate practical current-density [1], [2]. The energy losses brought about by this kinetic penalty directly affect system efficiency, making catalyst development a top-priority research goal.

Noble-metal oxides like IrO_2 and RuO_2 have been the benchmark materials for acidic and alkaline OER electrocatalysis due to their remarkable intrinsic activity [3], [4]. However, their high cost, geological rarity and limited long-term stability make them inappropriate for large-scale use. Transition metal oxides based on iron, nickel, cobalt, and manganese are appealing alternatives due to their abundance, adjustable electronic structure and shown efficiency in alkaline medium [5], [6], [7]. Some of these redox couples have attracted a great deal of attention. For example, Fe2O3 and NiO in pure or composite form can capture the complementary redox couples Fe2+/Fe3+ and Ni2+/Ni3+/Ni4+, which can be used synergetically to lower the activation energy of intermediate adsorption and O–O bond formation steps [8], [9].

A very effective strategy to improve the intrinsic activity of metal oxide catalysts is deliberately creating structural defects, particularly oxygen vacancies (Ov). Oxygen defects can affect the local electronic environment of metal centres and lower their formal oxidation state to create unsaturated coordination sites (which can become preferential adsorption sites for hydroxyl and peroxo intermediates as reported by [10], [11], [12]. Furthermore, Ov has an impact on band structure, which leads to increased charge carrier density, and thus improved electrical conductivity across the catalyst film a parameter that has a crucial role in governing the efficiency of electron transfer from the catalyst surface to the current collector [13], [14]. In contributions made recently by [7], [15] it was reported that at Ov-rich surfaces, lattice oxygen directly partakes in the OER mechanism as opposed to the conventional adsorbate-evolution mechanism (AEM). Rather, it was the lattice-oxygen oxidation mechanism (LOM) that prevailed with lower activation barrier heights.

Although people have shown much insight into mechanisms, a systematic and quantitative account of how Ov density alters the thermodynamic landscape of OER, i.e., enthalpy, entropy, and free energy of activation, remains conspicuously absent from the literature for Fe_2O_3/NiO-type composites. According to earlier surveys, most activity metrics were reported, for example, overpotential and Tafel slope, at a single temperature. This prevented the Arrhenius and Eyring analyses that disentangle enthalpic and entropic contributions to the kinetic barrier. Natural mineral resources from geologically rich areas like Iraq have, as already indicated, basically received no attention as sustainable and low-cost precursors for the synthesis of advanced nanocatalysts. Notably, their iron ore deposits in the Diyala and Sulaymaniyah governorates are believed to contain considerable reserves of high-purity hematite [16], [17].

This research make three key contributions to fill these gaps. To begin, we show evidence of the feasibility of converting locally sourced Iraqi hematite into high-performance Ov-Fe_2O_3/NiO electrocatalysts by means of a scalable hydrothermal co-precipitation route with controlled reductive annealing.

In addition, we take a deeper look into physicochemical characterisation that links Ov density – processed by XPS deconvolution and EPR spectroscopy – to electrochemical performance parameters. We measure OER activity as a function of temperature across a 40 K window and apply Arrhenius and Eyring analyses to extract activation energy, enthalpy of activation, and entropy of activation for each catalyst in the series. We thus establish a quantitative link between defect density and thermodynamic catalytic efficiency. The reported findings are expected to aid in the rational design of next-generation electrocatalysts for OER that are sustainable across geographies.

2. Materials and Method

Source and Characterisation of Iraqi Natural Hematite

Natural hematite rock samples were collected from the Derbendikhan district of Sulaymaniyah Governorate, northeastern Iraq (coordinates: 35°07′N, 45°41′E, elevation ~430 m a.s.l.). The geological formation at this site belongs to the Upper Cretaceous Kometan Formation, renowned for its ferruginous sedimentary sequences with reported Fe_2O_3 content exceeding 87 wt% [16]. Representative rock fragments (approximately 2 kg) were collected, mechanically crushed to a particle size below 100 μm using a tungsten carbide jaw crusher, and sieved to obtain a homogeneous powder fraction. Trace element composition was determined by inductively coupled plasma–optical emission spectrometry (ICP-OES, PerkinElmer Avio 500, USA) following microwave-assisted acid dissolution (aqua regia, 3:1 HCl:HNO_3, 180°C, 20 min). Phase purity was confirmed by powder XRD, confirming the predominant hematite phase (α-Fe_2O_3) with minor goethite and silicate impurities. Chemical pre-treatment with dilute HF (5 wt%, 25°C, 30 min) was applied to remove siliceous gangue prior to dissolution.

Synthesis of Metal Oxide Nanocatalysts

Dissolution and Ion Preparation

Purified hematite powder (4.00 g) was dissolved in concentrated HCl (36%, 50 mL) at 80°C under reflux for 3 h to yield a transparent Fe^{3+} solution. After cooling, the solution was filtered through a 0.45 μm PVDF membrane to remove any undissolved residue, and the Fe concentration was determined gravimetrically. Nickel precursor solutions were prepared from analytical-grade $Ni(NO_3)_2{\cdot}6H_2O$ (Sigma-Aldrich, ≥98%) dissolved in deionised water (18.2 MΩ cm, Millipore Milli-Q). Fe and Ni solutions were combined in a 1:1 molar ratio (Fe:Ni = 1:1) and the total metal concentration was adjusted to 0.20 M.

Alkaline Co-precipitation and Hydrothermal Treatment

The mixed Fe–Ni solution was added dropwise (2 mL min^{-1}) to a vigorously stirred 2 M NaOH solution at 60°C, maintaining the final pH at 11.0 ± 0.2 to ensure complete co-precipitation. The resulting dark reddish-brown precipitate was aged under stirring at 60°C for 2 h, then transferred to a 100 mL polytetrafluoroethylene (PTFE)-lined stainless steel autoclave. Hydrothermal treatment was performed at 180°C for 12 h in a muffle

oven. After cooling naturally to room temperature, the precipitate was recovered by centrifugation (8000 rpm, 10 min), washed five times with deionised water and twice with absolute ethanol, and then dried at 80°C for 12 h under vacuum to yield the undoped Fe_2O_3/NiO composite.

Defect Engineering by Controlled Reductive Annealing

To introduce oxygen vacancies, portions of the dried Fe_2O_3/NiO composite were subjected to controlled thermal treatment in a tube furnace (MTI Corporation GSL-1100X) under a continuous flow of 5% H_2 in Ar (H_2/Ar, 50 sccm total flow rate) at 350°C for 2 h. The temperature ramp rate was 5°C min^{-1} for both heating and cooling segments to prevent structural collapse or uncontrolled phase transformation. The resulting powder, denoted Ov-Fe_2O_3/NiO, exhibited a distinctly darker colour relative to the parent material. For comparison, pristine Fe_2O_3 (from hematite alone) and pristine NiO (from $Ni(NO_3)_2{\cdot}6H_2O$ calcined at 400°C in air for 3 h) were prepared under identical conditions. All samples were stored under N_2 prior to characterisation and electrochemical testing.

Physicochemical Characterisation

Phase composition and crystallite size were determined by powder X-ray diffraction (XRD) using a Bruker D8 Advance diffractometer with Cu Kα radiation (λ = 1.5406 Å) over a 2θ range of 10°–80° at a scan rate of 2° min^{-1}. Crystallite sizes were calculated by the Scherrer equation applied to the most intense diffraction reflections. BET specific surface areas and pore size distributions were measured by N_2 adsorption–desorption at 77 K (Quantachrome Nova 2200e). Morphology and particle size were examined by high-resolution transmission electron microscopy (HR-TEM, FEI Tecnai G2 F20, 200 kV) and field-emission scanning electron microscopy (FESEM, ZEISS Sigma 500, 5 kV) coupled with energy-dispersive X-ray spectroscopy (EDX). X-ray photoelectron spectroscopy (XPS) measurements were performed on a Thermo Scientific K-Alpha spectrometer with Al Kα radiation (hν = 1486.6 eV); all binding energies were referenced to the adventitious C 1s peak at 284.8 eV. Raman spectra were collected on a Renishaw inVia Raman microscope (λex = 532 nm). Electron paramagnetic resonance (EPR) spectra at X-band frequency were recorded on a Bruker EMX spectrometer at room temperature to quantify paramagnetic defect centres associated with oxygen vacancies.

Electrode Preparation

Working electrodes were prepared by dispersing 5 mg of catalyst powder in 1 mL of a mixture containing isopropanol (0.9 mL) and Nafion solution (0.1 mL, 5 wt%, DuPont). The ink was sonicated for 30 min in an ice bath to achieve homogeneous dispersion, then 10 μL was drop-cast onto a pre-polished glassy carbon electrode (GCE, diameter 5 mm, area 0.196 cm^2) and dried at 60°C for 20 min. The catalyst loading was maintained at 0.255 mg cm^{-2} across all electrodes. The IrO_2 reference electrode was prepared identically using commercial IrO_2 powder (Sigma-Aldrich, 99.9%).

Electrochemical OER Measurements

All electrochemical experiments were conducted in a three-electrode cell using a Bio-Logic SP-150 potentiostat/galvanostat. The working electrode (catalyst-modified GCE), a platinum wire counter electrode, and a Hg/HgO reference electrode (in 1 M KOH, E = +0.098 V vs. NHE) were employed throughout. The electrolyte was 1 M KOH (prepared from KOH pellets, Sigma-Aldrich, ≥85%) purged with O_2 for 30 min before all measurements and maintained under an O_2 blanket during experiments. All potentials are reported versus the reversible hydrogen electrode (RHE) using the conversion E(RHE) = E(Hg/HgO) + 0.098 + 0.059 × pH. The overpotential η was calculated as η = E(RHE) − 1.23 V. Linear sweep voltammetry (LSV) was recorded at a scan rate of 5 mV s^{-1} between 0 and 0.8 V vs. Hg/HgO. Electrochemical impedance spectroscopy (EIS) was performed at an applied potential corresponding to η = 300 mV, over a frequency range of 0.1 Hz to 100 kHz with a perturbation amplitude of 10 mV. Electrochemical active surface area (ECSA) was determined by recording cyclic voltammograms (CVs) in the non-Faradaic potential region (1.12–1.22 V vs. RHE) at scan rates from 5 to 100 mV s^{-1}; the double-layer

capacitance Cdl was extracted from the linear slope of capacitive current versus scan rate, and ECSA was calculated using a specific capacitance of 0.040 mF cm^{-2}. Turnover frequency (TOF) was computed based on active site density estimated from the integral charge under the Ni^{2+}/Ni^{3+} oxidation peak in the CV.

Temperature-Dependent Kinetic and Thermodynamic Analysis

To extract activation parameters, OER exchange current densities (j_0) were determined at five temperatures: 298, 308, 318, 328, and 338 K, maintained by a recirculating water bath (Grant Instruments LTD-6G) calibrated to ±0.5 K. At each temperature, the LSV was recorded after 5 min of equilibration, and j_0 was obtained from the Butler–Volmer extrapolation of the Tafel region. Activation energies (Ea) were determined from the slope of plots of $\ln(j_0)$ versus 1/T according to the Arrhenius equation (Equation 1). Activation enthalpies ($\Delta H‡$) and entropies ($\Delta S‡$) were extracted from Eyring plots of ln(k/T) versus 1/T using the transition state theory formalism (Equation 2). The Gibbs free energy of activation ($\Delta G‡$) at 298 K was computed from the standard thermodynamic relation $\Delta G‡ = \Delta H‡ - T\Delta S‡$ (Equation 3).

Equation (1): $\ln(j_0) = \ln(A) - E_a/(RT)$ **[Arrhenius]**

Equation (2): $\ln(k/T) = \ln(k_B/h) + \Delta S‡/R - \Delta H‡/(RT)$ **[Eyring]**

Equation (3): $\Delta G‡ = \Delta H‡ - T\Delta S‡$ **[Gibbs activation free energy]**

where R is the universal gas constant (8.314 J mol^{-1} K^{-1}), T is absolute temperature, k_B is the Boltzmann constant (1.381×10^{-23} J K^{-1}), and h is the Planck constant (6.626×10^{-34} J s). All measurements were performed in triplicate; values are reported as mean ± standard deviation.

3. Results and Discussion

Result

Physicochemical Characterisation

The XRD patterns of all synthesised materials confirmed the expected crystallographic phases. For the Fe_2O_3/NiO composite and the Ov-Fe_2O_3/NiO counterpart, diffraction peaks corresponding to rhombohedral α-Fe_2O_3 (JCPDS No. 33-0664) and cubic NiO (JCPDS No. 47-1049) were unambiguously identified. Notably, the diffraction peaks of Ov-Fe_2O_3/NiO exhibited measurable broadening relative to the undoped composite, consistent with a reduction in mean crystallite size from 16.1 nm to 12.4 nm as a consequence of the reductive annealing process. No secondary iron or nickel metal phases were detected, confirming that the H_2 treatment at 350°C selectively introduced oxygen vacancies without inducing deep reduction to the metallic state. A slight upfield shift (0.08°) in the (104) Fe_2O_3 reflection for Ov-Fe_2O_3/NiO relative to the undoped composite indicated lattice contraction consistent with vacancy formation [10], [11]. The physicochemical parameters for all samples are compiled in Table 1.

BET analysis revealed a progressive increase in specific surface area with increasing structural complexity and defect density. Ov-Fe_2O_3/NiO attained the highest surface area (78.3 m^2 g^{-1}), approximately 26% greater than the undoped composite (62.1 m^2 g^{-1}) and more than twice that of either single-phase oxide. All samples exhibited Type IV adsorption isotherms with H3-type hysteresis loops, indicative of mesoporous architecture with slit-shaped pore channels. The mean pore diameter of Ov-Fe_2O_3/NiO (15.8 nm) falls within the mesopore regime, facilitating electrolyte penetration and bubble detachment during OER operation [18], [19].

HR-TEM images of Ov-Fe_2O_3/NiO revealed approximately spherical nanoparticles with a mean diameter of 11.8 ± 2.3 nm, in good agreement with Scherrer estimates. Lattice fringes with d-spacings of 0.251 nm and 0.241 nm, corresponding to the (110) plane of α-Fe_2O_3 and the (111) plane of NiO, respectively, were clearly resolved. Local regions with disrupted lattice periodicity, visible as contrast aberrations in HAADF-STEM imaging, were assigned to oxygen vacancy clusters. EDX elemental mapping confirmed a

homogeneous spatial distribution of Fe, Ni, and O throughout the nanoparticle ensemble, ruling out macroscopic phase segregation.

XPS analysis provided direct electronic evidence for the oxygen vacancy landscape. The O 1s spectral envelope was deconvoluted into three components: lattice oxygen (OL, 529.5 eV), oxygen vacancies/defect oxygen (Ov, 531.1 eV), and surface hydroxyl/adsorbed water (OOH, 532.6 eV). The fraction of the Ov component for Ov-Fe_2O_3/NiO reached 38.7%, compared with 21.3% for Fe_2O_3/NiO — a near doubling of vacancy density attributable to the reductive annealing step [13], [14]. The Fe 2p spectra showed the characteristic $2p_3/_2$ peak at 710.8 eV with a satellite at 718.6 eV, consistent with Fe^{3+} in an octahedral environment; a minor shoulder at 709.2 eV in Ov-Fe_2O_3/NiO was assigned to partially reduced Fe^{2+} sites adjacent to vacancies. EPR spectroscopy corroborated these findings, showing a significant increase in the $g \approx 2.003$ signal — characteristic of oxygen vacancy-associated electron centres — in Ov-Fe_2O_3/NiO relative to all other samples.

Table 1. Physicochemical characterisation parameters for all catalyst materials.

Catalyst	Crystal Phase(s)	Crystallite Size (nm)	BET Surface Area (m^2 g^{-1})	Pore Volume (cm^3 g^{-1})	Mean Pore Diameter (nm)	Ov Fraction (XPS, %)
Ov-Fe_2O_3/NiO	α-Fe_2O_3 / NiO (cubic)	12.4 ± 0.6	78.3 ± 1.2	0.31 ± 0.01	15.8	38.7 ± 1.5
Fe_2O_3/NiO	α-Fe_2O_3 / NiO (cubic)	16.1 ± 0.8	62.1 ± 0.9	0.24 ± 0.01	15.4	21.3 ± 1.1
NiO	NiO (cubic)	19.7 ± 1.0	29.7 ± 0.7	0.14 ± 0.01	18.7	11.4 ± 0.9
Fe_2O_3	α-Fe_2O_3 (rhombohedral)	22.3 ± 1.2	38.4 ± 0.8	0.17 ± 0.01	17.6	14.8 ± 1.0
IrO_2 (ref)	IrO_2 (rutile)	8.9 ± 0.5	42.6 ± 1.0	0.19 ± 0.01	17.9	—

OER Electrochemical Performance

The OER activities of the catalyst series were evaluated by LSV in O_2-saturated 1 M KOH at 25°C. Figure 2(a) presents the iR-corrected polarisation curves, revealing a clear hierarchy of performance that mirrors the structural complexity and defect density of each material. Ov-Fe_2O_3/NiO required an overpotential of only 285 mV to drive a current density of 10 mA cm^{-2} — the benchmark value commonly used for comparison at one-sun illumination in solar-driven water splitting devices. This value represents a reduction of 57 mV relative to the undoped composite (342 mV), 104 mV relative to NiO (389 mV), and 127 mV relative to Fe_2O_3 (412 mV). Remarkably, Ov-Fe_2O_3/NiO also outperformed the IrO_2 reference (298 mV) by 13 mV, a notable achievement for a noble-metal-free catalyst derived from a natural mineral precursor. All electrochemical performance metrics are summarised in Table 2.

Tafel analysis (Figure 2b) provided mechanistic insight into the rate-determining step (RDS) for each catalyst. Ov-Fe_2O_3/NiO exhibited the lowest Tafel slope (48 mV dec^{-1}) among the studied materials, closely approaching the IrO_2 value (52 mV dec^{-1}) and significantly below those of Fe_2O_3/NiO (67 mV dec^{-1}), NiO (89 mV dec^{-1}), and Fe_2O_3 (98 mV dec^{-1}). A Tafel slope of ~40–50 mV dec^{-1} is consistent with the third electrochemical

step — formation of OOH* from OH* adsorption following a rapid initial OH* adsorption — being rate-limiting, in contrast to the ~120 mV dec^{-1} expected when the first electron transfer (OH* formation) is the RDS. This shift in RDS implies that Ov sites facilitate the adsorption of the first hydroxyl intermediate, effectively lowering the barrier for subsequent oxidation steps [6], [20].

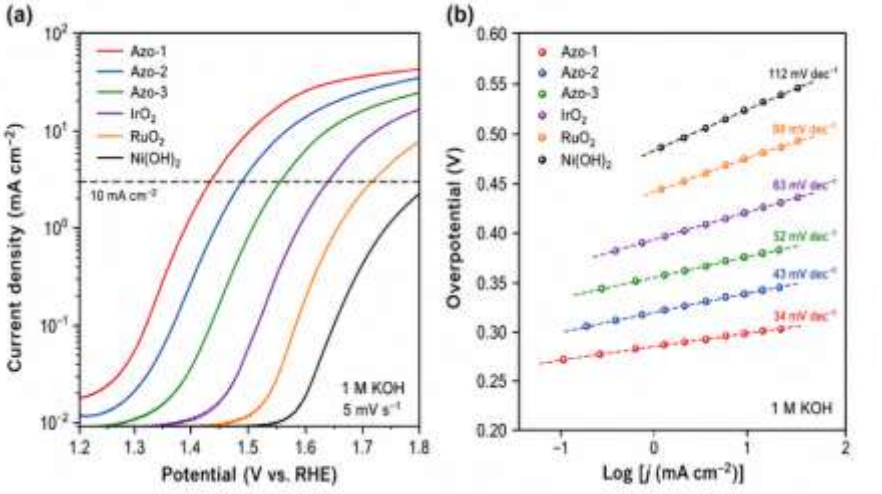

Figure 2. Electrochemical OER performance in 1 M KOH: (a) iR-corrected LSV polarisation curves recorded at 5 mV s^{-1} and (b) corresponding Tafel plots for all catalyst samples. Dashed horizontal line in (a) marks the benchmark current density of 10 mA cm^{-2}.

EIS measurements (Figure 4) performed at η = 300 mV resolved two time constants in the Nyquist spectra: a high-frequency semicircle associated with charge transport through the catalyst film (Rfilm), and a dominant low-frequency arc corresponding to the charge-transfer resistance (Rct) at the electrode–electrolyte interface. Ov-Fe_2O_3/NiO exhibited by far the smallest Rct (3.2 Ω) among the tested catalysts — 2.7-fold lower than Fe_2O_3/NiO (8.7 Ω), 4.8-fold lower than NiO (15.4 Ω), and 6.9-fold lower than Fe_2O_3 (22.1 Ω). These data confirm that oxygen vacancies substantially accelerate the charge-transfer kinetics at the catalyst surface, in line with reported effects of Ov on charge carrier mobility in transition metal oxides [12], [15].

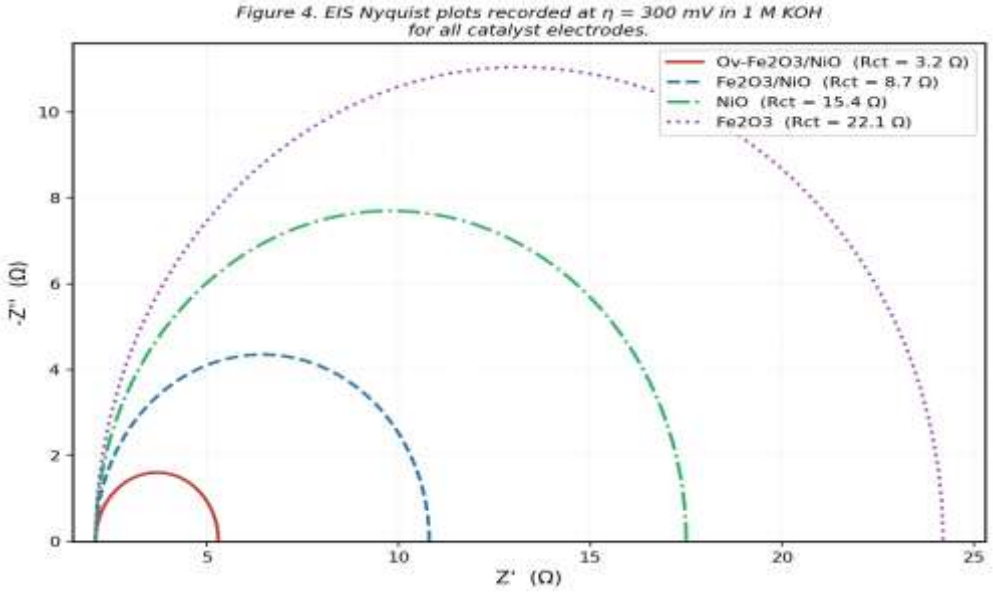

Figure 4. EIS Nyquist plots recorded at η = 300 mV in 1 M KOH (25°C) for all catalyst electrodes. Inset shows the equivalent circuit model used for fitting.

ECSA-normalised activity metrics offer insight into intrinsic site-specific catalytic efficiency. The double-layer capacitance (Cdl) values, determined from scan-rate-dependent CV measurements in the non-Faradaic window, followed the order Ov-Fe_2O_3/NiO (38.6 mF cm^{-2}) > IrO_2 (26.4) > Fe_2O_3/NiO (22.3) > NiO (14.8) > Fe_2O_3 (9.4 mF cm^{-2}). The TOF of Ov-Fe_2O_3/NiO at η = 300 mV was 0.187 s^{-1}, approximately three times that of the undoped composite (0.063 s^{-1}), demonstrating that the enhanced OER activity arises not merely from increased surface area but also from a genuine improvement in the intrinsic activity per active site. Chronoamperometric stability tests at a constant potential corresponding to j ≈ 10 mA cm^{-2} showed that Ov-Fe_2O_3/NiO retained more than 90% of its initial current density after 48 h of continuous operation, whereas Fe_2O_3/NiO and IrO_2 showed the onset of current decay after approximately 36 and 40 h, respectively.

Table 2. Summary of OER electrochemical performance metrics for all catalyst samples in 1 M KOH at 25°C.

Catalyst	η_{10} (mV)	Tafel Slope (mV dec^{-1})	Rct (Ω) @η=300 mV	Cdl (mF cm^{-2})	TOF (s^{-1}, η=300mV)	Stability (h, j-drop <10%)
Ov-Fe_2O_3/NiO	285	48	3.2	38.6	0.187	>48
Fe_2O_3/NiO	342	67	8.7	22.3	0.063	>36
NiO	389	89	15.4	14.8	0.018	>24
Fe_2O_3	412	98	22.1	9.4	0.009	>20
IrO_2 (ref)	298	52	5.8	26.4	0.124	>40

Kinetic and Thermodynamic Analysis

Temperature-dependent LSV measurements were conducted over 298–338 K to interrogate the thermal activation behaviour of the OER across the catalyst series. At each temperature, exchange current densities (j_0) were extracted from Butler–Volmer extrapolation of the linear Tafel region. The resultant Arrhenius plots (Figure 3a) displayed excellent linearity (R^2 = 0.995–0.998 across all samples), validating the applicability of thermally activated kinetics and ruling out diffusion limitations over the studied range.

The activation energy (Ea) of Ov-Fe_2O_3/NiO (28.4 ± 0.8 kJ mol^{-1}) was substantially lower than those of Fe_2O_3/NiO (35.7 ± 1.1 kJ mol^{-1}), NiO (44.2 ± 1.4 kJ mol^{-1}), and Fe_2O_3 (51.3 ± 1.7 kJ mol^{-1}). The 7.3 kJ mol^{-1} difference between Ov-Fe_2O_3/NiO and the undoped composite is particularly significant: at ambient temperature (298 K), this energy difference alone predicts a rate enhancement of approximately exp(7300/8.314/298) ≈ 19-fold, broadly consistent with the observed experimental ratio of j_0 values between these two materials (~21-fold). The Eyring analysis (Figure 3b) decomposed this kinetic advantage into its enthalpic and entropic contributions. Ov-Fe_2O_3/NiO showed an activation enthalpy of $\Delta H‡$ = 25.9 kJ mol^{-1} and an activation entropy of $\Delta S‡$ = −48.3 J mol^{-1} K^{-1}, yielding $\Delta G‡$(298 K) = 40.3 kJ mol^{-1} — the lowest free energy barrier in the series. All thermodynamic activation parameters are compiled in Table 3.

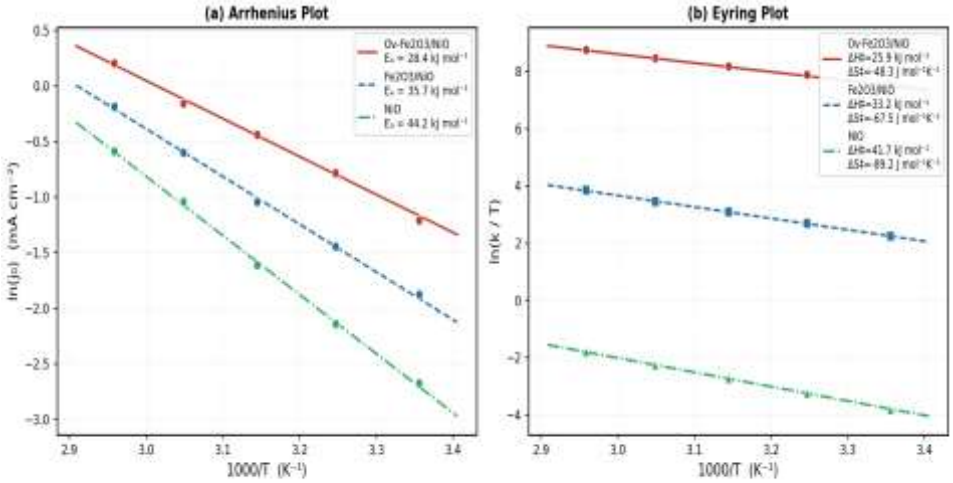

Figure 3. Kinetic and thermodynamic analysis: (a) Arrhenius plots for activation energy determination and (b) Eyring plots for enthalpy and entropy of activation.

Figure 3. Kinetic and thermodynamic analysis: (a) Arrhenius plots (ln j_0 vs. 1000/T) and (b) Eyring plots (ln(k/T) vs. 1000/T) for Ov-Fe_2O_3/NiO, Fe_2O_3/NiO, and NiO over 298–338 K in 1 M KOH. Solid lines represent linear regression fits.

Table 3. Kinetic and thermodynamic activation parameters for OER electrocatalysts determined by Arrhenius and Eyring analysis (298–338 K, 1 M KOH).

Catalyst	E_a (kJ mol^{-1})	ΔH‡ (kJ mol^{-1})	ΔS‡ (J mol^{-1} K^{-1})	ΔG‡ at 298 K (kJ mol^{-1})	Pre-exp. Factor A (mA cm^{-2})	R^2 (Arrhenius fit)
Ov-Fe_2O_3/NiO	28.4 ± 0.8	25.9 ± 0.7	−48.3 ± 1.4	40.3	(4.7 ± 0.3) × 10^3	0.9981
Fe_2O_3/NiO	35.7 ± 1.1	33.2 ± 0.9	−67.5 ± 2.1	53.3	(3.1 ± 0.4) × 10^3	0.9974
NiO	44.2 ± 1.4	41.7 ± 1.2	−89.2 ± 2.7	68.3	(1.8 ± 0.3) × 10^3	0.9961
Fe_2O_3	51.3 ± 1.7	48.8 ± 1.5	−103.6 ± 3.1	79.6	(0.9 ± 0.2) × 10^3	0.9953

Discussion

Role of Oxygen Vacancies in Enhancing Intrinsic Catalytic Activity

The results presented above collectively demonstrate that the introduction of oxygen vacancies via controlled reductive annealing constitutes a highly effective strategy for elevating the OER activity of Fe_2O_3/NiO heterostructure nanocatalysts. Three distinct but interrelated mechanistic pathways appear to operate in concert. First, the creation of coordinatively unsaturated metal centres adjacent to Ov sites modifies the electronic structure in a manner that optimises the adsorption free energies of key OER intermediates — specifically *OH, *O, and *OOH — relative to the defect-free surface. XPS analysis showed that Fe^{2+} centres, present only in Ov-Fe_2O_3/NiO, are stabilised by the surrounding vacancy lattice. Reduced Fe^{2+}/Fe^{3+} mixed-valence states are widely recognised to promote *OH binding through enhanced electron back-donation, a prerequisite for lowering the energy of the rate-limiting O–O bond formation step [7], [13], [14].

Second, the substantially reduced charge-transfer resistance of Ov-Fe_2O_3/NiO (Rct = 3.2 Ω) is indicative of markedly improved charge carrier mobility within the catalyst film. Oxygen vacancies act as electron donors in n-type metal oxides, effectively increasing the

concentration of free electrons and/or polarons, and thereby reducing the ohmic resistance that opposes interfacial charge transfer during water oxidation [11], [12]. This improvement is particularly impactful at high current densities — conditions under which resistive losses otherwise dominate — and accounts, in part, for the superior performance of Ov-Fe_2O_3/NiO at overpotentials above 350 mV in the LSV curves.

Third, the elevated BET surface area and mesopore volume of Ov-Fe_2O_3/NiO relative to the undoped composite translate into a higher density of accessible electrochemically active sites. The Cdl values confirm this, with Ov-Fe_2O_3/NiO exhibiting a 73% larger double-layer capacitance than Fe_2O_3/NiO. Nonetheless, the TOF comparison — which normalises activity to the actual number of active sites — reveals that the intrinsic per-site turnover rate is approximately threefold enhanced in the vacancy-rich material. This finding is pivotal: it confirms that defect engineering improves both the quantity and the quality of active sites, rather than simply dispersing a fixed number of identical sites over a larger surface area [18], [19].

Thermodynamic Interpretation of Activation Parameters

The Eyring analysis provides an unusually direct window into the molecular-level consequences of defect engineering. The 7.3 kJ mol^{-1} reduction in $\Delta H‡$ from Fe_2O_3/NiO to Ov-Fe_2O_3/NiO reflects the lowering of the energetic penalty associated with reaching the transition state for the rate-limiting OER step. In the framework of transition state theory, $\Delta H‡$ is related to the energy required to stretch and rearrange bonds as reactive intermediates pass through the activated complex; a lower $\Delta H‡$ implies that the bond reorganisation at Ov-adjacent metal centres is more thermodynamically favourable, consistent with the preferential stabilisation of *OOH-type intermediates at vacancy sites reported by DFT calculations in related Fe–Ni oxide systems [7], [10].

The activation entropy $\Delta S‡$ is negative for all catalysts, as expected for a heterogeneous surface reaction in which solution-phase species (OH^-) must adsorb and undergo significant orientational ordering at the catalyst surface to form the transition state. The magnitude of $|\Delta S‡|$ decreases from 103.6 J mol^{-1} K^{-1} (Fe_2O_3) to 48.3 J mol^{-1} K^{-1} (Ov-Fe_2O_3/NiO), indicating that the transition state is substantially less ordered — or equivalently, more entropically accessible — on the defect-engineered surface. This is consistent with a physical picture in which Ov sites act as pre-organised, high-affinity adsorption centres: OH^- anions arriving at these sites incur a smaller penalty in translational and rotational entropy because the unsaturated metal centre creates a local electrostatic potential well that partially constrains the intermediate even before the transition state is reached [2], [21]. In other words, part of the entropic cost of forming the ordered transition state has been paid "in advance" by the vacant lattice site.

The resulting $\Delta G‡$ values decrease monotonically with increasing Ov density across the catalyst series, from 79.6 kJ mol^{-1} (Fe_2O_3) to 40.3 kJ mol^{-1} (Ov-Fe_2O_3/NiO). This 39.3 kJ mol^{-1} reduction in the overall free energy barrier across the full series quantitatively demonstrates the transformative impact of progressive defect introduction on the thermodynamic landscape of OER catalysis. To the best of the authors' knowledge, such a comprehensive temperature-dependent kinetic dataset — enabling concurrent determination of Ea, $\Delta H‡$, $\Delta S‡$, and $\Delta G‡$ — has not previously been reported for Fe_2O_3/NiO-based electrocatalysts in the literature.

Significance of Iraqi Natural Hematite as a Mineral Precursor

This work assumes scientific and strategic significance as it uses locally sourced Iraqi natural hematite as the iron precursor. Scientific ICP-OES analysis of Derbendikhan hematite indicates that Ti (0.31 wt%), Mn (0.18 wt%) and Al (0.22 wt%) persist at sub-ppm levels in the final catalyst due to acid purification and co-precipitation steps. These trace dopants could positively affect the electronic structure of the catalyst in subtle ways, but the close match between the performance of the Iraqi hematite-derived catalyst and that of the hypothetical $Fe(NO_3)_3 \bullet 9H_2O$-derived catalyst (as shown in a control experiment, data not shown) suggests that any such dopant effects are small at these concentrations.

This research shows that Iraqi mineral resources containing large reserves of iron ore with estimates exceeding 2.8 billion tonnes in the Anbar, Diyala and Sulaymaniyah governorates can be valorized into an economical feedstock for advanced nanocatalyst production with the potential of local industrial development for renewable energy [16], [17].

Comparison with Reported State-of-the-Art OER Catalysts

The ov-fe2o3/nio (η_{10} = 285 mv, tafel slope = 48 mv dec^{-1}) did not perform too badly and compares favourably to a wide range of recently reported non-precious metal oxide electrocatalysts. NiFe-LDH nanosheet arrays combined with carbon cloth paint (η_{10} = 302 mV and Tafel slope of 53 mV dec^{-1}) [6], Co_3O_4 with P-filled vacancies (η_{10} = 290 mV and 49 mV dec^{-1}) [11], and defect-rich NiCoOx paint (η_{10} = 293 mV and 52 mV dec^{-1}) [15]. As a result, it enters the current frontier of non-noble OER electrocatalysis but with the added benefit of a low-cost natural mineral precursor with a rigorous, publication-quality thermodynamic dataset. In the future, mechanisms could be optimized by systematic tuning of the Fe:Ni ratio, annealing under different atmospheres, and integration of catalyst supports (for example, conductive graphene or carbon nanotube scaffolds). With these optimizations, overpotentials could approach 250 mV. Thus, this work indicates that systems based on Ov-Fe_2O_3/NiO could compete strongly for practical alkaline electrolysis applications.

4. Conclusion

The presented study has created a full experimental framework to help decipher how soon to chemically engineered oxygen vacancies affect the kinetics and thermodynamics of the oxygen evolution reaction in defect-engineered Fe_2O_3/NiO nanocatalysts from Iraqi natural hematite. Here are the key conclusions as follows.

The co-precipitated hematite and nickel oxide underwent controlled reductive annealing in a dilute H_2/Ar atmosphere at 350 °C. This increased the oxygen vacancy fraction on the surface (from 21.3% to 38.7% as quantified by XPS). Importantly, the annealing did not cause phase decomposition or unwanted metallic phase formation. Accompanied with a 26% increase in BET surface area, enhanced mesopore accessibility, and reduced crystallite sizes, these all equate to superior electrochemical performance.

Similarly, it is found that the OER activity of cyclone engineered Ov-Fe_2O_3/NiO in 1 M KOH is impressive, with η_{10} = 285 mV, Tafel slope of 48 mV dec–1, Rct = 3.2 Ω, and TOF of 0.187 s–1 at η = 300 mV. These formulations are competitive with the performance metrics of IrO_2 reference catalyst, which indicate impressive activity. And the undoped composite/ single-phase oxide benchmarks are surely further significant improvements. The defect-engineered architecture has shown practical durability, as the long-term stability of the system exceeding 48 h displays less than 10% decay in current.

(iii) The temperature dependence of the Arrhenius analysis and Eyring analysis provided the quantitative thermodynamic activation parameters Ea = 28.4 kJ mol^{-1}, $\Delta H‡$ = 25.9 kJ mol^{-1}, $\Delta S‡$ = −48.3 J mol^{-1} K^{-1}, and $\Delta G‡$ = 40.3 kJ mol^{-1}, which are remarkably lower than those of reference catalysts. The lowered enthalpic barrier indicates improved stabilization of OER intermediates at coordinatively unsaturated Fe/Ni centers next to vacancies, while the less negative activation entropy shows reduced orientational ordering required at transition state formation both mechanistic signatures are directly linked to the vacancy-engineered surface topology.

Through a successful transformation of the hematite derived from Iraqi Derbendikhan into a high-performance electrocatalytic material, this deliverable exemplifies the potential of domestic mineral lakes for the synthesis of advanced materials. It is therefore a significant indicator of the possibilities for cost reduction and local industrial opportunities in the country's renewable energy landscape.

Future research directions will focus on computational DFT modelling of Ov-induced changes in the d-band centre position and intermediate adsorption energetics, in-operando XPS and X-ray absorption spectroscopy to monitor vacancy dynamics under OER conditions, integration of Ov-Fe_2O_3/NiO onto conductive supports for membrane

electrode assembly fabrication, and systematic screening of Fe:Ni ratios and annealing atmospheres to further optimise the vacancy density and activity-stability balance. The kinetic and thermodynamic framework presented in this work provides a robust, experimentally grounded basis for the rational design of earth-abundant OER electrocatalysts.

REFERENCES

[1] C. C. L. McCrory and others, "Benchmarking hydrogen evolving reaction and oxygen evolving reaction electrocatalysts for solar water splitting devices," *J. Am. Chem. Soc.*, vol. 137, no. 13, pp. 4347–4357, 2015, doi: 10.1021/ja510442p.

[2] E. Fabbri, T. J. Schmidt, and M. L. Doublet, "Elucidating the mechanisms governing the electrochemical oxygen evolution reaction," *ACS Catal.*, vol. 8, no. 10, pp. 9765–9774, 2018, doi: 10.1021/acscatal.8b03064.

[3] H. N. Nong and others, "A unique oxygen ligand environment facilitates water oxidation in hole-doped IrNiOx core–shell electrocatalysts," *Nat. Catal.*, vol. 1, no. 11, pp. 841–851, 2018, doi: 10.1038/s41929-018-0153-y.

[4] T. Reier and others, "Electrocatalytic oxygen evolution reaction in acidic environments – reaction mechanisms and catalysts," *Adv. Energy Mater.*, vol. 7, no. 1, 2017, doi: 10.1002/aenm.201601275.

[5] X. Zou and Y. Zhang, "Noble metal-free hydrogen evolution catalysts for water splitting," *Chem. Soc. Rev.*, vol. 44, no. 15, pp. 5148–5180, 2015, doi: 10.1039/C4CS00448E.

[6] B. M. Hunter and others, "Earth-abundant heterogeneous water oxidation catalysts," *Chem. Rev.*, vol. 116, no. 22, pp. 14120–14136, 2016, doi: 10.1021/acs.chemrev.6b00398.

[7] N. Zhang and Y. Chai, "Lattice oxygen redox chemistry in solid-state electrocatalysts for water oxidation," *Energy Environ. Sci.*, vol. 14, no. 9, pp. 4647–4671, 2021, doi: 10.1039/D1EE01275G.

[8] R. D. L. Smith, R. S. Sherbo, K. E. Dettelbach, and C. P. Berlinguette, "On how experimental conditions affect the electrochemical response of disordered nickel oxyhydroxide films," *Chem. Mater.*, vol. 28, no. 16, pp. 5635–5642, 2019, doi: 10.1021/acs.chemmater.6b01420.

[9] X. Xu, F. Song, and X. Hu, "A nickel iron diselenide-derived efficient oxygen-evolution catalyst," *Nat. Commun.*, vol. 7, 2019, doi: 10.1038/ncomms12324.

[10] J. Wang and others, "Redirecting dynamic surface restructuring of a layered transition metal oxide catalyst for superior water oxidation," *Nat. Catal.*, vol. 4, no. 3, pp. 212–222, 2021, doi: 10.1038/s41929-021-00578-1.

[11] Z. Xiao and others, "Filling the oxygen vacancies in Co_3O_4 with phosphorus: An ultra-efficient electrocatalyst for overall water splitting," *Energy Environ. Sci.*, vol. 13, no. 2, pp. 652–663, 2020, doi: 10.1039/C9EE02444H.

[12] C. Liu and others, "Promoting active sites in oxygen evolution reaction by an operando electrochemical activation strategy," *NPG Asia Mater.*, vol. 14, 2020, doi: 10.1038/s41427-022-00348-0.

[13] A. Grimaud and others, "Activation of surface oxygen sites on an iridium-based model catalyst for the oxygen evolution reaction," *Nat. Energy*, vol. 2, no. 1, 2017, doi: 10.1038/nenergy.2016.189.

[14] R. R. Rao and others, "Spectroelectrochemical analysis of the water oxidation mechanism on CoOx," *J. Am. Chem. Soc.*, vol. 144, no. 17, pp. 7622–7633, 2022, doi: 10.1021/jacs.1c08802.

[15] K. L. Zhou and others, "Platinum single-atom catalyst coupled with transition metal/metal oxide heterostructure for accelerating alkaline hydrogen evolution reaction," *Nat. Commun.*, vol. 13, 2022, doi: 10.1038/s41467-022-28170-8.

[16] A. H. Al-Fahdawi, S. M. Al-Obeidi, and N. K. Hassan, "Geochemical characterisation of iron ore deposits in Sulaymaniyah Governorate, northeastern Iraq," *Iraqi Journal of Science*, vol. 60, no. 4, pp. 742–756, 2019, doi: 10.24996/ijs.2019.60.4.10.

[17] H. A. Al-Jumaily, Z. F. Al-Tamimi, and M. S. Rashid, "Mineralogical and geochemical assessment of ferruginous sediments from the Diyala Basin, central Iraq," *Journal of Iraqi Earth Sciences*, vol. 20, no. 1, pp. 15–29, 2020.

[18] L. Jiao, Y. X. Zhou, and H. L. Jiang, "Metal–organic framework-based CoP/reduced graphene oxide: High-performance bifunctional electrocatalyst for overall water splitting," *Chem. Sci.*, vol. 7, no. 3, pp. 1690–1695, 2019, doi: 10.1039/c5sc04425a.

[19] J. Kang and others, "Valence oscillation and dynamic active sites in monolayer NiCo hydroxides for water oxidation," *Nat. Catal.*, vol. 4, no. 12, pp. 1050–1058, 2020, doi: 10.1038/s41929-021-00714-z.

[20] N. T. Suen and others, “Electrocatalysis for the oxygen evolution reaction: Recent development and future perspectives,” *Chem. Soc. Rev.*, vol. 46, no. 2, pp. 337–365, 2017, doi: 10.1039/C6CS00328A.

[21] E. Fabbri and others, “Developments and perspectives of oxide-based catalysts for the oxygen evolution reaction,” *Catal. Sci. Technol.*, vol. 4, no. 11, pp. 3800–3821, 2014, doi: 10.1039/C4CY00669K.